ACS Partner Journal

CHEMICAL & BIOMEDICAL IMAGING

pubs.acs.org/ChemBioImaging

Article

Alteration of Lipid Metabolism in Hypoxic Cancer Cells

Gil A. Gonzalez, Ezinne U. Osuji, Natalie C. Fiur, Matthew G. Clark, Seohee Ma, Laura L. Lukov, and Chi Zhang*

Cite This: *Chem. Biomed. Imaging* 2025, 3, 25−34

Read Online

ACCESS | Metrics & More | Article Recommendations | Supporting Information

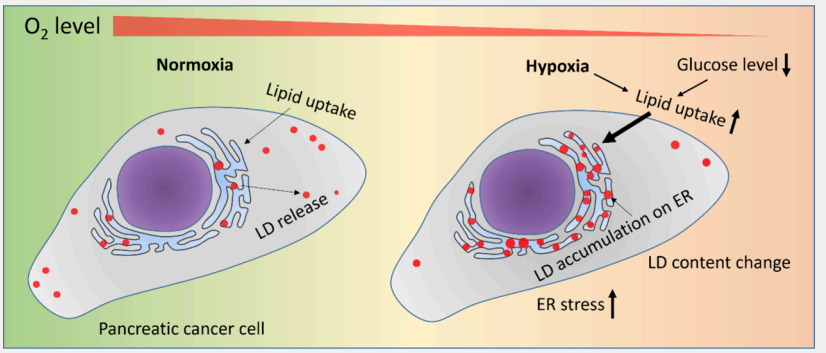

ABSTRACT: Due to uncontrolled cell proliferation and disrupted vascularization, many cancer cells in solid tumors have limited oxygen supply. The hypoxic microenvironments of tumors lead to metabolic reprogramming of cancer cells, contributing to therapy resistance and metastasis. To identify better targets for the effective removal of hypoxia-adaptive cancer cells, it is crucial to understand how cancer cells alter their metabolism in hypoxic conditions. Here, we studied lipid metabolic changes in cancer cells under hypoxia using coherent Raman scattering (CRS) microscopy. We discovered the accumulation of lipid droplets (LDs) in the endoplasmic reticulum (ER) in hypoxia. Time-lapse CRS microscopy revealed the release of old LDs and the reaccumulated LDs in the ER during hypoxia exposure. Additionally, we explored the impact of carbon sources on LD formation and found that MIA PaCa2 cells preferred fatty acid uptake for LD formation, while glucose was essential to alleviate lipotoxicity. Hyperspectral-stimulated Raman scattering (SRS) microscopy revealed a reduction in cholesteryl ester content and a decrease in lipid saturation levels of LDs in hypoxic MIA PaCa2 cancer cells. This alteration in LD content is linked to reduced efficacy of treatments targeting cholesteryl ester formation. This study unveils important lipid metabolic changes in hypoxic cancer cells, providing insights that could lead to better treatment strategies for hypoxia-resistant cancer cells.

KEYWORDS: *hypoxia, cancer, Raman, microscopy, lipid droplets, endoplasmic reticulum, live cell, nutrition*

INTRODUCTION

In the case of extreme proliferation, many cancer cells in solid tumors face a limited oxygen supply. This hypoxic microenvironment contributes to metabolic reprogramming that makes cancer cells resistant to treatment and promotes metastasis.[1] Hypoxia-inducible factors (HIFs) play key roles in regulating hypoxia-related metabolic responses. While extensive studies have focused on HIF-activation-induced carbohydrate metabolic switches,[2−4] changes in lipid metabolism in hypoxia only attracted attention in recent years.[5−8] Lipids are critical for energy production, membrane synthesis, and cell signaling. Low oxygen conditions significantly impact mitochondrial activity and lipid metabolism.[5−8]

Hypoxia tends to increase lipid uptake and synthesis in cancer cells via activating HIFs. For example, HIF-1α has been reported to activate peroxisome proliferator-activated receptor gamma (PPARγ) which enhances lipid uptake and triacylglycerol (TAG) *de novo* synthesis.[9] HIF-1α also promotes the expression of fatty acid binding protein (FABP) that increases cellular lipid uptake and storage in human trophoblasts,[10] breast cancer cells,[11] and hepatocytes.[12] The enhanced lipid uptake and synthesis might contribute to cellular stress and cytotoxicity.

To avoid lipid-induced cytotoxicity, cancer cells convert fatty acids to neutral lipids and store them in lipid droplets (LDs).[13] LDs are organelles responsible for both the storage and metabolism of neutral lipids.[14,15] They are synthesized and released from the endoplasmic reticulum (ER) and then transported along microtubules for degradation.[16] LD

Received: July 2, 2024
Revised: October 4, 2024
Accepted: October 8, 2024
Published: October 21, 2024

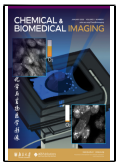

membrane proteins such as lipases are commonly involved in neutral lipid metabolism. LDs are commonly found in many cancer cells and are linked to altered lipid metabolism in cancer.[17,18]

The impact of hypoxia and HIFs on LD formation and accumulation in cancer cells has been studied by conventional biochemical assays. For example, HIF-1 has been found to stimulate lipin 1 expression, promoting LD accumulation in hepatoblastoma and cervical adenocarcinoma cells.[7] Additionally, HIF-1 increases the expression of acylglycerol-3-phosphate acyltransferase 2 (AGPAT2), an enzyme involved in TAG biosynthesis.[19] This metabolic change contributes to chemotherapy resistance of hepatocellular carcinoma cell lines.[19] Furthermore, HIF-2α activation elevates LD membrane protein perilipin-2 (PLIN2), enhancing lipid storage in LDs in cancer cells.[20] PLIN2-dependent lipid storage plays a role in maintaining ER homeostasis and preventing ER stress in clear-cell renal cell carcinoma cells.[20] Moreover, hypoxia reduces the activity of enzymes associated with lipid catabolism, such as carnitine palmitoyltransferase 1A (CPT1A)[21] and medium- and long-chain acyl-CoA dehydrogenases (MCAD and LCAD),[22] resulting in elevated LD accumulation in cancer cells. Collectively, these metabolic switches lead to increased LD accumulation in cancer cells under hypoxic conditions. Despite the studies mentioned above, the changes in LD amount, content, and distribution in hypoxic cancer cells, particularly at the single-cell level, remain elusive. A better understanding of subcellular LD characteristics could provide new insights into hypoxia-induced cancer metabolic alteration and support the development of more effective treatment strategies for hypoxia-resistant cancer cells.

Coherent Raman scattering (CRS) microscopy, including coherent anti-Stokes Raman scattering (CARS) and stimulated Raman scattering (SRS), provides excellent contrast for visualizing LDs.[23] SRS microscopy has revealed changes in LD content, such as an increase in cholesteryl ester in prostate cancer cells[24] and a decrease in lipid saturation levels in mesenchymal melanoma cells[25] and ovarian cancer stem cells.[26] Additionally, *de novo* synthesis of neutral lipids from glucose has been visualized using isotope tracing together with SRS microscopy.[27] LD dynamics can also be traced and quantified by both CARS and SRS.[28−30] Despite CRS microscopy being extensively applied to study LD characteristics in various conditions, to the best of our knowledge, it has not been utilized to understand changes in the LD amount, distribution, and contents induced by hypoxia exposure.

In this work, we utilized CRS spectroscopy and microscopy to investigate the changes in LD distribution and content in hypoxic cancer cells, focusing on pancreatic cancer cells. Using SRS, we discovered ER-associated LD accumulation in these cells under hypoxic conditions. Time-lapse epi-CARS imaging of the same field-of-view (FOV) revealed the release of old LDs and the reaccumulation of new LDs in the ER. Additionally, we studied the carbon sources for LD synthesis and found that for MIA PaCa2 cells, lipid uptake is the preferred pathway for LD formation, while glucose is essential for mitigating lipotoxicity. Using hyperspectral SRS microscopy, we discovered a decrease in cholesteryl ester content and lipid saturation in LDs of hypoxic MIA PaCa2 cancer cells. This study provides new insights into the reprogramming of lipid metabolism in pancreatic cancer cells under hypoxic conditions.

EXPERIMENTAL SECTION

Hyperspectral Stimulated Raman Scattering Microscopy and Multimodal Imaging

The configuration of the SRS microscope used in this study has been detailed in previous publications and will not be extensively described here.[31,32] Briefly, its hyperspectral capability is achieved through spectral focusing of broadband femtosecond laser pulses. An InSight X3+ femtosecond laser, with a fixed output at 1045 nm and a tunable output ranging from 690 to 1300 nm at an 80 MHz repetition rate, serves as the laser source. The 1045 nm laser output is used as the Stokes beam, while the other laser output turned to 802 nm is used as the pump beam. The pump and Stokes pulses are chirped to 3.4 and 1.8 ps, respectively, by using SF-57 glass rods.[31] The laser pulses are focused onto the sample using either a 60× (UPlanSApo, 60×/1.2 W) or a 40× (LUMPLFLN 40×/0.80 W) water dipping objective lens. The microscope has an upright configuration. SRS signals are acquired in the forward direction using a customized photodiode (PD) paired with a lock-in amplifier (HF2LI, Zurich Instruments). The Stokes beam is modulated at approximately 2.4 MHz, while the pump beam is demodulated at the same frequency after PD detection. Additionally, the microscope features two epidetection channels for simultaneously measuring two-photon excitation fluorescence (TPEF) signals from the sample at center wavelengths of approximately 450 and 570 nm. Photomultiplier tubes (PMTs, H7422-40, Hamamatsu) are used for fluorescence signal detection. In the forward direction, a PMT is also available for forward CARS signal detection. This upright multimodal imaging system is not compatible with real-time and time-lapse imaging of live cells in a hypoxic environment. The upright SRS/CARS/TEPF microscope has a limited working distance when using water dipping objectives. This configuration does not allow integration with a standard stage-top incubator, preventing long-term imaging of live cells within the same FOV.

Coherent-Anti-Stokes Raman Scattering Microscopy for Time-Lapse Hypoxia Study

To enable long-term time-lapse monitoring of LD metabolism in the same FOV in hypoxia, we designed an epi-CARS modality on an inverted microscope (IX71, Olympus) that is compatible with a stage-top incubator (WSKMX with STX-CO2O2, Tokai Hit) for long-term CARS imaging. The gas controller allows for creating an O_2 environment ranging from 0.1% to 20% while maintaining a 5% CO_2 level. The incubator also regulates humidity and keeps the temperature at 37 °C for cell culture. The excitation lasers for CARS are sourced from the same laser used in the SRS modality but are unchirped and maintained at ∼120 fs for epi-CARS excitation. The power at the sample is 20 mW for both the pump and Stokes beams. A PMT is placed in the epi-direction to acquire CARS signals generated from the sample. A dichroic beam splitter separates and directs the CARS signals from the excitation beams to the PMT. The same 60× water dipping objective lens is used to focus the laser pulses onto the sample. To prevent water evaporation, a water-matching liquid (Cargille Laboratories, 20114) was applied between the objective lens and the sample dish. The operation of the laser and imaging system can be remotely controlled.

Cell Culture

MIA PaCa2 and HeLa cells were obtained from ATCC and cultured in Dulbecco's Modified Eagle Medium (DMEM) containing 4 mg/mL glucose, glutamine, and 10% fetal bovine serum (FBS) as the control group. The cells were first seeded into glass-bottom dishes and grown to 30−50% confluency in a standard CO_2 incubator set at 37 °C and 5% CO_2. For the normoxia condition, the cells were maintained in the same culture environment. For the hypoxia condition, the cells were cultured in a stage-top incubator (WSKMX with STX-CO2O2, Tokai Hit) with 0.1% O_2 for various durations. To study the impact of different carbon sources, we created different nutritional conditions using normal DMEM with 4 mg/mL glucose, glucose-free DMEM, and glucose-free and glutamine-free DMEM,

https://doi.org/10.1021/cbmi.4c00050
Chem. Biomed. Imaging 2025, 3, 25−34

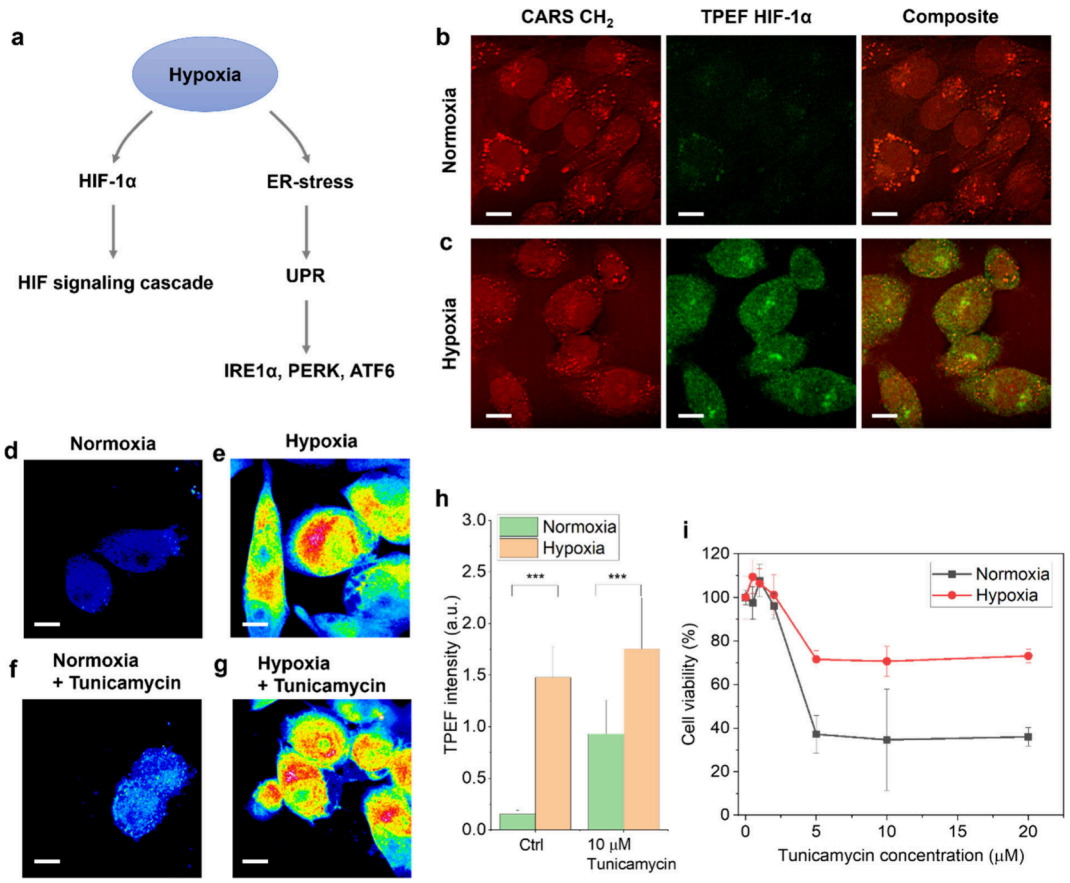

Figure 1. Validation of hypoxia conditions via protein expression analysis. (a) Hypoxia-induced changes in HIF-1α expression and ER stress markers. UPR: unfolded protein response. IRE1α, PERK, and ATF6 are common ER stress marker proteins. (b) CARS and TPEF imaging of MIA PaCa2 cells under normoxia. The CARS signals are generated at the 2855 cm^{-1} Raman shift. The TPEF signals result from immunofluorescence labeling of HIF-1α at 570 nm, excited by both 800 and 1045 nm laser pulses. (c) Similar to panel b but following 24-h hypoxia exposure. (d, e) Immunofluorescence imaging of PERK in MIA PaCa2 cells under normoxia and after 24-h hypoxia exposure, respectively. (f, g) Similar to panels d and e, cells are treated with 10 μM tunicamycin for a 24-h duration. (h) Quantitative analysis of the fluorescence signal levels from panels d–g. (i) MTT cell viability results of MIA PaCa2 cells treated with varying concentrations of tunicamycin under normoxia and hypoxia conditions. Scale bars: 10 μm. ***p-value $\leq$0.001.

along with or without FBS in different combinations. For the deuterated glucose treatment and C–D imaging, MIA PaCa2 cells were cultured in DMEM media devoid of glucose and supplemented with 4.5 mg/mL deuterated glucose (d_7-glucose, Sigma-Aldrich). For immunofluorescence and hyperspectral SRS studies, the cells were fixed using 10% formalin.

Cell Viability Study

Cell viability was measured using an MTT assay. Cells were seeded in 96-well plates and allowed to attach to the bottom of the dish under normal culture conditions. The plates were then treated with different concentrations of drugs or nutrition conditions and cultured in the CO_2 incubator in normoxia or exposed to hypoxia in the stage-top incubator for different lengths of time. Tetrazolium bromide was dissolved in the culture medium at a concentration of 5 mg/mL. Ten microliters of tetrazolium bromide solution was added to each well and allowed to incubate with cells for 2 h. Then the medium from each well was removed and replaced with 100 μL of dimethylsulfoxide (DMSO). The optical density values at 570 nm were measured using a plate reader (SmartReader 96, Accuris Instruments). Six replicates were performed for each condition on the same 96-well microplates to produce the error bar in cell viability or density plots.

Fluorescence Labeling

For immunofluorescence labeling of HIF-1α, the primary anti-HIF 1α antibody (GTX127309, GeneTex) was used at a dilution of 1:200 with the secondary antibody, goat anti-rabbit IgG H&L Alexa Fluor 488 (ab150077, Abcam), at a dilution of 1:200. The secondary antibody was illuminated by 800 nm femtosecond laser pulses, and fluorescence signals were acquired using the 570 nm channel. For labeling protein kinase RNA-like ER kinase (PERK), the primary antibody (PA5-99447, Thermo Fisher Scientific) was used at a dilution of 1:200 with a goat anti-rabbit IgG H&L Alexa Fluor 488 (ab150077, Abcam) secondary antibody at a dilution of 1:200. The immunofluorescence sample preparation followed a standard protocol. Goat serum was used as the blocking buffer. For ER-Tracker labeling, 200 nM ER-Tracker Green (Thermo Fisher Scientific) was incubated with live cells for 30 min before imaging.

Image and Spectral Analysis

Images were acquired using lab-designed software based on LABVIEW. The images were saved in TXT format and processed using ImageJ. Images were converted to different color schemes for better display. Contrasts were adjusted to show details of cells for all imaging modalities. For the nutrition studies, the same contrast levels were applied to all conditions. For hyperspectral SRS (HSRS) image analysis, 200 image frames were acquired to generate the SRS spectra. LD masks were obtained using the method illustrated in the Supporting Information. The mask was then applied to the original HSRS images to obtain the average SRS spectra from LDs. Spectra were normalized by dividing the maximum value. A more detailed explanation of the HSRS spectral analysis method can be found in the Supporting Information (Figure S1). For the statistical analysis, four

https://doi.org/10.1021/cbmi.4c00050
Chem. Biomed. Imaging 2025, 3, 25–34

images were used for each condition. Each image measures 30 × 30 μm^2 area and contains approximately 3−4 cells.

For PERK fluorescence signal quantification made in Figure 1, seven images were analyzed in each condition. The image size is 60 × 60 μm^2, and each image contains 1−8 cells. For the quantification of LDs inside ER made in Figure 2, six images were used in each condition, with each having a size of 50 × 50 μm^2. For analyzing the LD amount and size in Figure 4, three larger images, each measuring about 200 × 200 μm^2, were used. These larger images contain 80−300 cells, depending on the nutritional conditions and oxygen levels.

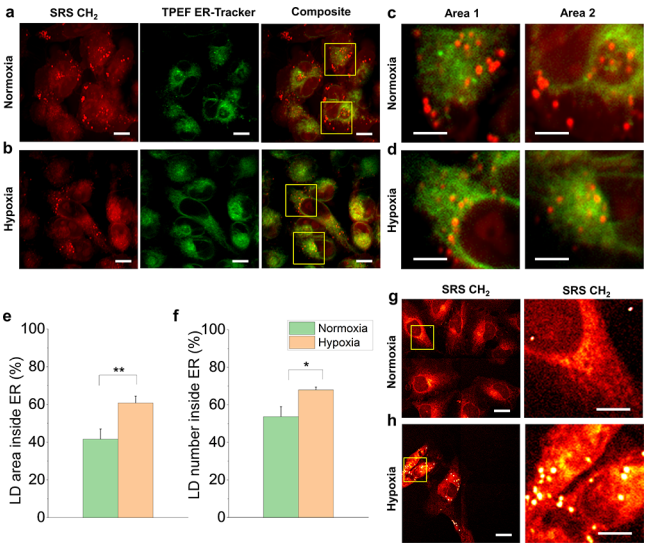

Figure 2. Lipid droplet (LD) accumulation in the endoplasmic reticulum (ER) in hypoxia. (a) SRS signals at 2855 cm^{-1} and TPEF signals at 570 nm from ER Tracker for MIA PaCa2 cells in normoxia. The composite image overlays the two contrasts from the same field of view. (b) Similar to panel a but following 24-h hypoxia exposure. (c, d) Magnified views of the outlined areas in panels a and b, respectively. (e, f) Quantification of the percentage of LD area inside ER over the total LD area, and the number of LDs inside ER over the total number of LDs, for MIA PaCa2 cells. (g, h) SRS images of HeLa cells in normoxia and hypoxia conditions measured at the 2855 cm^{-1} Raman shift. Scale bars: 10 μm for panels a, b, and left images in g, h; 5 μm for panels c, d, and right images in g, h. *0.01 ≤ p-value <0.05, **0.001 ≤ p-value <0.01.

RESULTS AND DISCUSSION

Confirming the Hypoxia Microenvironment

In this study, we create the hypoxia environment at 5% CO_2 concentration, 0.1% O_2 concentration, and 37 °C, and maintain cultured cancer cells in this environment using a stage-top incubator. It has been reported that hypoxia induces multiple metabolic and signaling alterations in cells, including the overexpression of HIF-1α and increased ER stress (Figure 1a). To confirm the creation and maintenance of a hypoxic environment using the stage-top incubator installed in our imaging system, we used immunofluorescence to label HIF-1α and compared normoxia and hypoxia conditions. Simultaneous CARS and TPEF imaging from the same FOV were performed for MIA PaCa2 cells. The laser wavelengths were tuned to CH_2 vibrations at 2855 cm^{-1} to visualize LDs and the overall cell morphology, while TPEF was used to image the fluorescently labeled HIF-1α proteins. We found that after 24 h of hypoxia exposure at a 0.1% O_2 level, strong fluorescence signals of HIF-1α were detected under hypoxia but not under normoxia (Figure 1b,c), highlighting the overexpression of HIF-1α in the hypoxic environment.

Furthermore, we used immunofluorescence to image and quantify the PERK protein level, a marker of ER stress,[33,34] and found a significant increase in PERK expression levels after hypoxia exposure (Figure 1d,e). A similar but less significant increase in PERK expression was found in normoxia when treating cells with the ER stress inducer tunicamycin at 10 μM final concentration (Figure 1f).[35] Interestingly, when treating hypoxic MIA PaCa2 cells with tunicamycin, the cells showed enhanced PERK expression compared to the normoxia condition, but similar levels of PERK expression to hypoxia without tunicamycin treatment (Figure 1g). Quantitative analysis of PERK fluorescence signals confirmed that both hypoxia and tunicamycin treatment can enhance ER stress. The cell viability analysis indicates that MIA PaCa2 cells in hypoxia were more resistant to tunicamycin-induced ER stress (Figure 1i). The cancer cells are more resistant to ER stressors in hypoxia is likely due to HIF-activated unfolded protein response (UPR), which could enhance chaperone expression that helps protein folding.[36] The metabolic switch from oxidative phosphorylation to enhanced glycolysis could also lower the production of reactive oxygen species (ROS) that might contribute to ER stress.[37−39] Collectively, these results confirm that our stage-top incubator can effectively create a hypoxic microenvironment for long-term culture and imaging.

LDs Accumulate in the ER in Hypoxia

To quantify and compare LD amounts and distributions in live cells under normoxia and hypoxia conditions, we applied SRS microscopy, tuning the laser wavelength to excite at 2855 cm^{-1}. The ER was labeled using an ER-Tracker fluorescent probe and visualized using the TPEF modality integrated with SRS. We found abundant LDs in MIA PaCa2 cells under both normoxia and hypoxia conditions (Figure 2a−d). However, a larger portion of LDs was colocalized with the ER in the hypoxia condition (Figure 2b,d). We quantified the total amount of LDs and the LDs that are located inside the ER using SRS and TPEF images. The masks of LDs are obtained using the method as illustrated in Figure S1. The mask of ER is obtained by TPEF images and performed AND calculation with the LD mask to obtain LDs inside ER. An example is illustrated in Figure S2. Quantitative analysis confirmed that both LD area percentage and the count of LDs inside the ER increased after 24 h of hypoxia exposure (Figure 2e,f). In contrast, the ER size showed no statistically significant change. This phenomenon was also observed in HeLa cells (Figure 2g,h). These results indicate that in hypoxia, LDs in cancer cells tend to redistribute and accumulate in the ER.

The upright SRS microscope does not permit long-term imaging of LD redistribution in live cells from the same FOV. High-resolution imaging requires water-dipping objective lenses with short working distances for tight laser focusing. However, dipping the objective lens into the culture dish necessitates removing the dish lid, leading to media evaporation and contamination, which compromises the long-term stability of the cell microenvironment. To solve this problem, we designed an epi-CARS platform based on an inverted microscope. The configuration of the epi-CARS microscope is shown in Figure 3a. This platform is compatible with the stage-top incubator, which can create and maintain normoxic or hypoxic microenvironments for cells. The objective lens remains outside of the culture chamber, allowing

https://doi.org/10.1021/cbmi.4c00050
Chem. Biomed. Imaging 2025, 3, 25−34

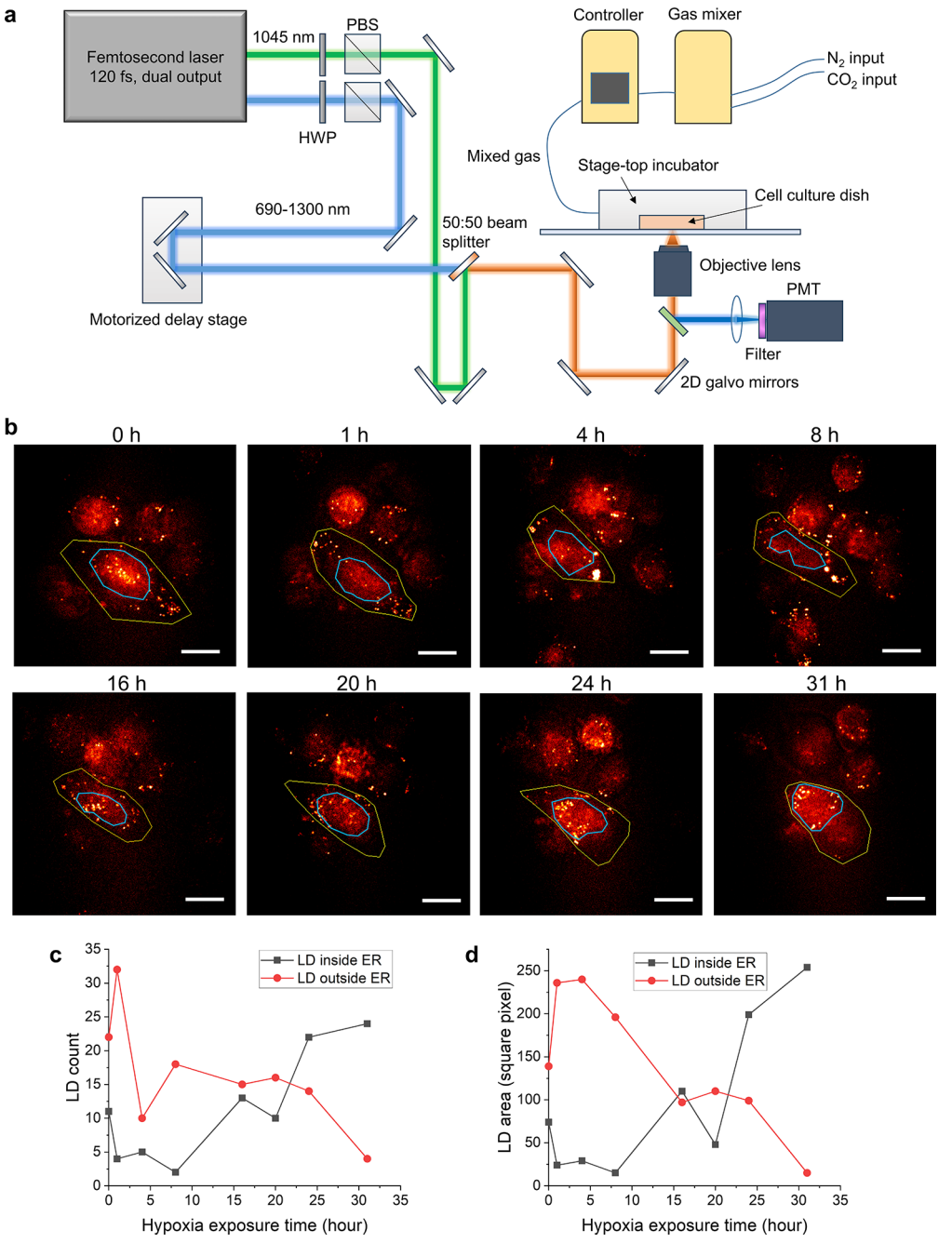

Figure 3. Time-lapse imaging of lipid droplet (LD) redistribution in live cells. (a) An epi-CARS microscope paired with a stage-top incubator designed to create and maintain a stable hypoxia microenvironment for time-lapse CARS measurement of LD redistribution in live cells. PBS: polarization beam splitter; HWP: half-wave plate; PMT: photomultiplier tube. (b) Time-lapse epi-CARS images at various time points, measured at the 2855 cm^{-1} Raman shift. The boundary of a cell and its ER area are outlined in yellow and blue, respectively. (c) Quantitative analysis of LD counts inside and outside ER. (d) Quantitative analysis of total LD areas inside and outside ER. LDs are initially released from the ER within the first hour of hypoxia exposure and then reaccumulate inside the ER after 24 h of hypoxia exposure. Scale bars: 10 μm.

for unperturbed imaging from the same FOV for over 72 h. To prevent contact water evaporation when using the water-dipping objective lens, an index-matching medium was applied. The CARS signals were separated by a dichroic beam splitter from the excitation lasers and sent to the PMT.

The epi-CARS configuration integrated with the hypoxia stage-top incubator allows for long-term monitoring of LD changes in cells from the same FOV. Long-term imaging was performed at 0, 1, 3, 4, 5, 6, 8, 16, 18, 20, 24, 25, 29, and 31 h. In Figure 3b, we display images from 8 selected time points, where the targeted cell remains within the FOV. To minimize photoperturbation to cell functions, only 10 image frames were continuously acquired at each time point with a pixel dwell time of 20 μs (see video in Supporting Information). As shown in Figure 3b, under the normoxic condition, LDs are found both inside and outside the ER. Due to their densely packed lipid-rich membranes, ERs exhibit stronger CH_2 symmetric stretching signals compared to other cell parts, except for LDs. Interestingly, we observed a rapid release of LDs from the ER to the cytosol after just 1 h of hypoxia exposure. The LDs

https://doi.org/10.1021/cbmi.4c00050
Chem. Biomed. Imaging 2025, 3, 25−34

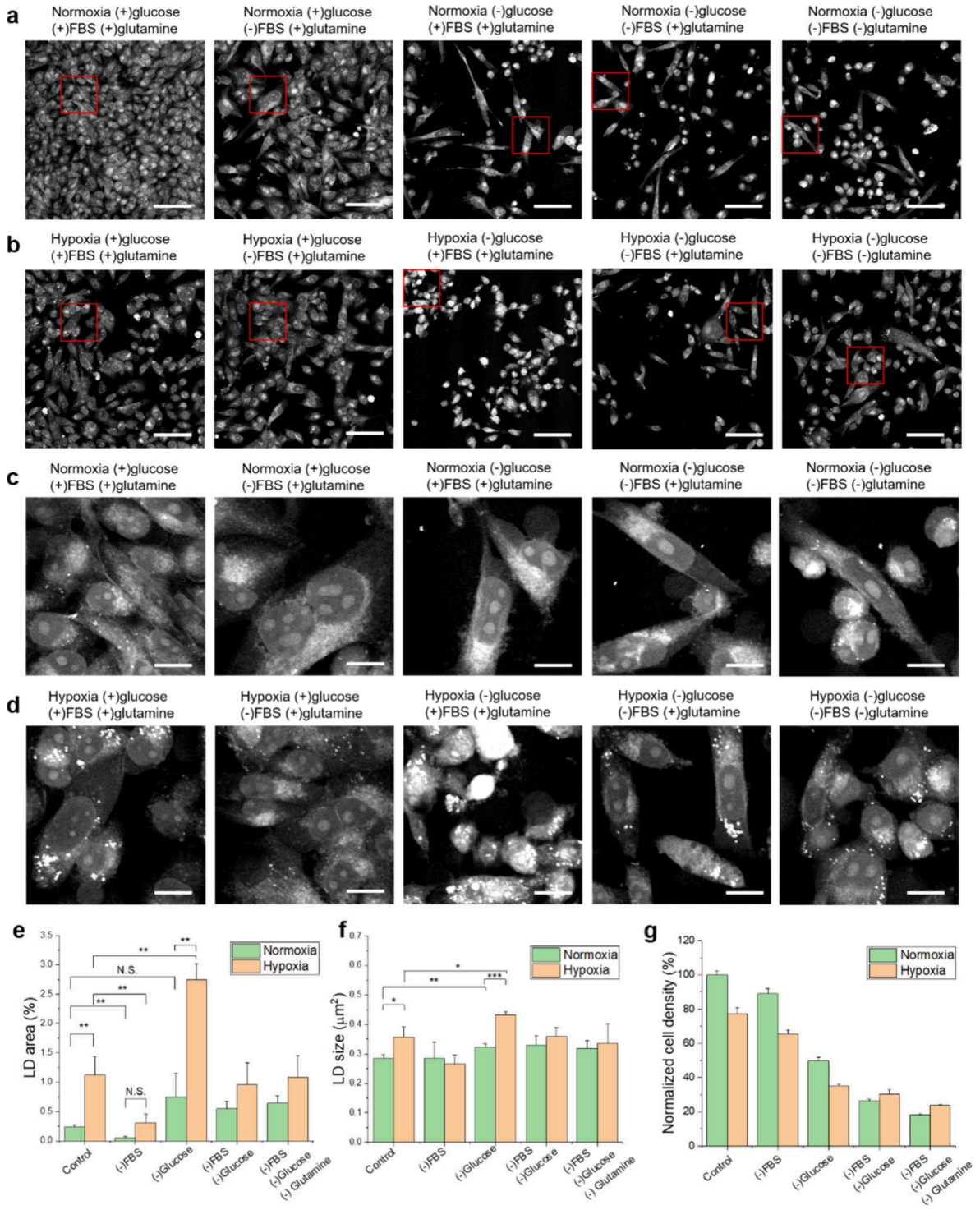

Figure 4. Nutritional effects on lipid droplet (LD) formation and cell viability. (a) SRS images of MIA PaCa2 cells at 2855 cm^{-1} under various nutritional conditions in normoxia. (b) SRS images of MIA PaCa2 cells at 2855 cm^{-1} under various nutritional conditions after 48-h hypoxia exposure. (c, d) Magnified images of outlined areas from panels a and b, respectively. Scale bars: 50 μm for panels a and b, 10 μm for panels c and d. (e) Quantitative LD area analysis by quantifying the percentage of LD area over the total cell area in various treatment conditions. (f) Quantification of LD size in various treatment conditions. (g) The normalized MIA PaCa2 cell density when cultured in various conditions with or without glucose, FBS, and glutamine in normoxia or hypoxia for 48 h. *0.01 ≤ p-value <0.05, **0.001 ≤ p-value <0.01, ***p-value <0.001.

reaccumulated in the ER after 24 h of hypoxia exposure (Figure 3b). To better illustrate the dynamic changes of LDs inside and outside the ER, we quantified the LD count and total LD area of the cell at eight time points, with results plotted in Figure 3c,d. At the 1-h time point, an increase in LDs outside the ER and a decrease in LDs inside the ER were detected (Figure 3c,d). The drop in LD count at the 3-h time point is attributed to LD aggregation, as observed in Figure 3b. Despite this drop in the LD count, the total LD area indicates no significant LD depletion at this time point. After 24 h, LDs inside the ER have significantly increased, while LDs outside the ER have markedly decreased (Figures 3c,d).

https://doi.org/10.1021/cbmi.4c00050
Chem. Biomed. Imaging 2025, 3, 25−34

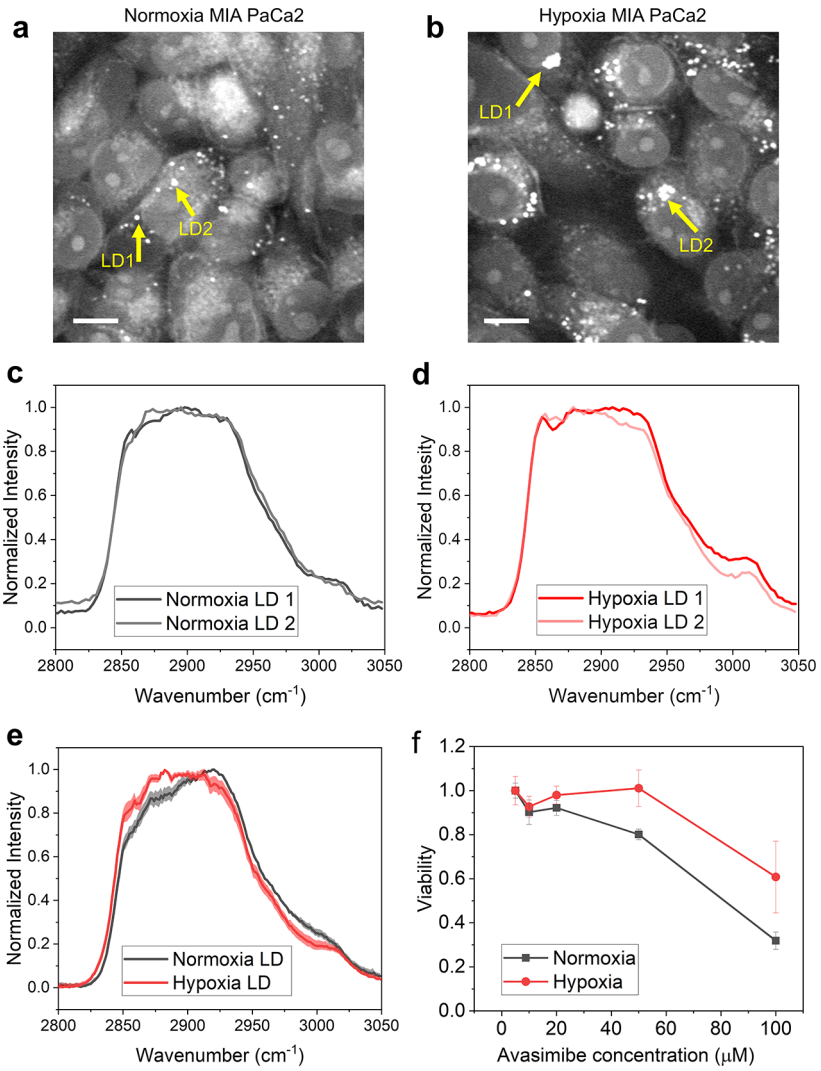

Figure 5. Changes in the lipid droplet (LD) content under hypoxia. (a, b) SRS images showing LDs in MIA PaCa2 cells under normoxia and hypoxia conditions, respectively. Arrows point to example LDs in each image. (c, d) SRS spectra in the C−H stretching regions from example LDs in each condition. (e) Averaged LD spectra from all LDs under normoxia and hypoxia conditions. (f) MTT cell viability results of MIA PaCa2 cells treated with different concentrations of avasimibe for 24 h under normoxia and hypoxia conditions. Scale bars: 10 μm.

ER is responsible for the synthesis of LDs. This time-lapse study indicates that the LDs in the ER under hypoxic conditions are newly synthesized after hypoxia exposure. The accumulation of LDs in the ER in hypoxia suggests that while LD synthesis continues, the release of LDs into the cytosol is impeded by the hypoxic condition. This phenomenon is likely influenced by the impact of hypoxia on key LD biogenesis proteins such as seipin. Seipin is critical for maintaining the LD morphology and converting nascent LDs to mature ones.[40,41] It was reported that in low oxygen conditions such as neuroinflammation induced by ischemic stroke, the seipin mRNA levels are significantly decreased.[42] The accumulation of LDs in the ER might be associated with elevated ER stress, as shown in Figure 1, or it could contribute to increased resistance to ER stress induced by tunicamycin. Future studies will further investigate the mechanisms of LD accumulation and the relationships between LD synthesis in the ER and ER stress.

Impact of Carbon Sources on LD Formation and Cell Viability

Understanding the impact of different carbon sources on the formation of LDs in cancer cells under normoxia and hypoxia is crucial. In our cell culture conditions, these carbon sources include glucose, lipids, and glutamine. FBS is the major lipid source while normal DMEM culture medium can supply both glucose and glutamine. Lipids for LD formation can be directly taken up by cells from the culture medium or synthesized using glucose or glutamine. We controlled the availability of glucose, lipids, and glutamine in the culture medium to explore their impact on cellular LD production. Cells treated with DMEM (4 mg/mL glucose and glutamine) and 10% FBS served as the control group. Four other groups were used, each with deprivation of glucose, FBS, glucose+FBS, and glucose+FBS +glutamine.

As shown in Figure 4, under the normal culture condition with all carbon sources available, MIA PaCa2 cells accumulate more LDs after 48 h of hypoxia exposure compared to normoxia. Both the total LD area and the average LD size increased in hypoxia (Figure 4e,f). MTT assay results, which

https://doi.org/10.1021/cbmi.4c00050
Chem. Biomed. Imaging 2025, 3, 25−34

measure total cell density, show a decrease in cell density under hypoxia in the normal culture medium (Figure 4g). Since no significant increase in dead cells was observed during imaging, the reduced cell count under hypoxia compared to normoxia is likely due to decreased proliferation of MIA PaCa2 cells upon HIF activation. It is well documented that HIF activation under hypoxia reduces cancer cell proliferation by affecting the electron transport chain, the Krebs cycle, and other metabolic pathways.[43,44]

When FBS is deprived, LD formation is significantly reduced in both normoxia and hypoxia conditions (Figure 4a–e), highlighting the importance of lipid uptake for LD formation in MIA PaCa2 cells. To verify glycolysis is involved in lipogenesis and LD synthesis, we used a glucose-free medium and added deuterated glucose (d_7-glucose) for cell culture. After 48 h, we detected CD signals from LDs in both conditions (Figure S3), indicating that glucose is involved in lipogenesis and LD formation. However, no significant difference in lipogenesis from glucose was observed between the hypoxia and normoxia conditions. We compared these deuterated C–D signals from MIA PaCa2 cells with those from HeLa cells. The HeLa cells showed much stronger C–D signals in the hypoxia condition compared to the normoxia condition (Figure S3). From these intensity levels, we conclude that for MIA PaCa2 cells, LD production from glucose is a less effective pathway compared to direct lipid uptake.

Conversely, under hypoxic conditions with glucose deprivation, LD accumulation significantly increased (Figure 4a–f) compared to both the control and FBS-deprived conditions. This suggests that in the absence of glucose, MIA PaCa2 cells have enhanced lipid uptake from FBS, contributing to elevated LD formation. Additionally, glucose deprivation leads to a significant decrease in cell density in both normoxia and hypoxia, as shown in Figure 4a–d and 4g, with many cells exhibiting a rounded shape and stronger C–H signals in SRS images. This morphological change and higher SRS C–H signals are associated with apoptosis.[45] This indicates that glucose deprivation results in a more pronounced reduction in MIA PaCa2 cell growth. Given the correlation between increased LD count and decreased cell density and viability, we hypothesize that elevated lipid uptake and LD accumulation in hypoxia, particularly inside the ER, contribute to increased cytotoxicity and reduced cancer cell proliferation and survival. When the deprivation of glucose is combined with the deprivation of FBS, or both FBS and glutamine, LD accumulation is still observed in MIA PaCa2 cells, especially under hypoxic conditions (Figure 4e). However, compared to glucose deprivation alone, in such conditions, LD accumulation is significantly reduced in hypoxia (Figure 4e).

The above results indicate that in hypoxia, MIA PaCa2 cells tend to slow down their proliferation and accumulate LDs. Direct lipid uptake is a preferred pathway for LD formation in these cells under hypoxic conditions, while glucose metabolism is also involved in LD synthesis in both conditions. This lipid accumulation can be potentially toxic to cancer cells, and the availability of glucose is essential to mitigate such lipotoxicity for MIA PaCa2 cells.

Alteration of LD Lipid Content in Hypoxia

Next, we studied changes in LD lipid contents under hypoxia using HSRS microscopy in the C–H stretching region. HSRS has been utilized to understand the content changes of neutral lipids in many biological systems.[25,46−49] We selected two LDs in MIA PaCa2 cells cultured in normoxia and hypoxia conditions and compared their SRS spectra. As shown in Figures 5a–d, a dip at 2870 cm^{-1}, indicating a decrease in cholesteryl ester content, was discovered under hypoxia.[50,51] The narrow peak shoulder between 2960 and 3000 cm^{-1} also indicates such a change in cholesteryl ester content.[25] Furthermore, we averaged the SRS spectra of all LDs in MIA PaCa2 cells in different FOVs under both normoxia and hypoxia conditions. The LD masks were selected based on their stronger SRS intensity at the 2855 cm^{-1} Raman transition. The averaged spectra show similar changes in the cholesteryl ester content (Figure 5e).

Acyl-coenzyme A: cholesterol acyltransferases-1 (ACAT-1), also known as sterol o-acyltransferase-1 (SOAT-1), the enzyme responsible for the accumulation of cholesteryl ester, has been reported as a potential target for killing prostate cancer cells.[24,52] Given the reduced cholesteryl ester content in hypoxic MIA PaCa2 cells, we hypothesize that drugs targeting ACAT-1 would be less effective for hypoxic cells. To test this, we treated MIA PaCa2 cells with avasimibe, an ACAT-1 inhibitor, under both normoxia and hypoxia conditions, and found that the hypoxic cells were more resistant to the treatment (Figure 5f). This further verifies the reduction of cholesteryl ester in LDs of hypoxic MIA PaCa2 cells.

Besides the cholesteryl ester content difference, an increase in the SRS spectra at 3010 cm^{-1} in hypoxia suggests a decrease in the saturation level of neutral lipids in hypoxia compared to normoxia (Figure 5c,d).[26,53] These changes indicate significant alterations in lipid metabolism for MIA PaCa2 cells in hypoxia. It has been reported that hypoxia inhibits the oxygen-dependent stearoyl-CoA desaturase (SCD) enzyme, leading to an increase in lipid saturation, particularly triglycerides, in kidney cancer cells.[54] However, we discovered the opposite change in lipid saturation levels in hypoxic pancreatic cancer cells. Such a decrease in lipid saturation is also detected in A549 cells after 48-h hypoxia exposure (Figure S4) but not in the HeLa cells (Figure S5). These results indicate that hypoxia-induced lipid content changes are cell-type dependent.

CONCLUSIONS

Using CRS microscopy, we discovered LD accumulation inside ER in MIA PaCa2 and HeLa cells under hypoxic conditions.

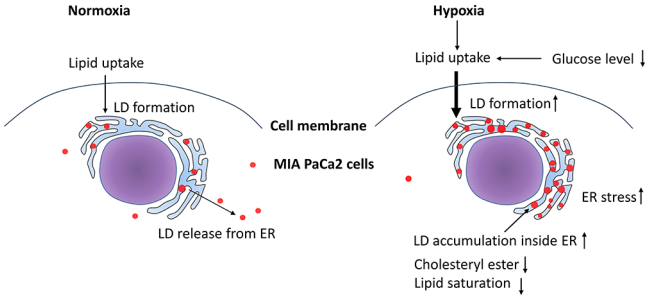

Figure 6. A schematic illustrating the changes in lipid uptake, LD formation, LD accumulation inside ER, and LD content changes induced by hypoxia.

Time-lapse CARS imaging revealed that LDs are first released and then reaccumulated inside the ER during hypoxia exposure. Furthermore, we found that MIA PaCa2 cells prefer lipid uptake for LD formation, while glucose is essential for alleviating lipotoxicity. HSRS microscopy unveiled changes in

https://doi.org/10.1021/cbmi.4c00050
Chem. Biomed. Imaging 2025, 3, 25−34

LD content under hypoxic conditions, including a reduction in cholesteryl ester composition and a decrease in lipid saturation level for MIA PaCa2 cells. The change in cholesteryl ester content correlates with the reduced efficacy of ACAT-1 targeting drugs for hypoxic cancer cells. A schematic of such lipid amount, distribution, and content changes is illustrated in Figure 6. Collectively, our study sheds new light on the changes in lipid metabolism in cancer cells under hypoxic conditions. This new understanding provides guidance for developing new treatment strategies to better target hypoxia-resistant cancer cells.

■ ASSOCIATED CONTENT

Supporting Information

The Supporting Information is available free of charge at https://pubs.acs.org/doi/10.1021/cbmi.4c00050.

Supplementary video 1, combined time-lapse epi-CARS images of LDs at different time points in hypoxia (AVI)

Supporting Figures S1−S5 (PDF)

■ AUTHOR INFORMATION

Corresponding Author

Chi Zhang − *Department of Chemistry, Purdue University, West Lafayette, Indiana 47907, United States; Purdue Center for Cancer Research, West Lafayette, Indiana 47907, United States; Purdue Institute of Inflammation, Immunology, and Infectious Disease, West Lafayette, Indiana 47907, United States;* orcid.org/0000-0002-7735-5614; Email: zhan2017@purdue.edu

Authors

Gil A. Gonzalez − *Department of Chemistry, Purdue University, West Lafayette, Indiana 47907, United States*

Ezinne U. Osuji − *College of Pharmacy, Purdue University, West Lafayette, Indiana 47907, United States; Purdue Center for Cancer Research, West Lafayette, Indiana 47907, United States*

Natalie C. Fiur − *Department of Chemistry, Purdue University, West Lafayette, Indiana 47907, United States; Purdue Center for Cancer Research, West Lafayette, Indiana 47907, United States*

Matthew G. Clark − *Department of Chemistry, Purdue University, West Lafayette, Indiana 47907, United States*

Seohee Ma − *Department of Chemistry, Purdue University, West Lafayette, Indiana 47907, United States*

Laura L. Lukov − *Department of Chemistry, Purdue University, West Lafayette, Indiana 47907, United States*

Complete contact information is available at: https://pubs.acs.org/10.1021/cbmi.4c00050

Author Contributions

C.Z. and G.A.G. designed the project. G.A.G., E.U.O., N.C.F. S.M. L.L.L, and C.Z. performed the experiments. G.A.G. and C.Z. conducted the data analysis. M.G.C. helped in CRS system alignment and maintenance. C.Z. obtained the funding and supervised the work.

Notes

The authors declare no competing financial interest.

■ ACKNOWLEDGMENTS

This work is supported by a pioneer grant from Purdue Center for Cancer Research and NIH R35GM147092.

■ REFERENCES

(1) Brahimi-Horn, M. C.; Chiche, J.; Pouysségur, J. Hypoxia and cancer. *J. Mol. Med.* **2007**, *85* (12), 1301−1307.

(2) Guillemin, K.; Krasnow, M. A. The hypoxic response: huffing and HIFing. *Cell* **1997**, *89* (1), 9−12.

(3) Xie, H.; Simon, M. C. Oxygen availability and metabolic reprogramming in cancer. *J. Biol. Chem.* **2017**, *292* (41), 16825−16832.

(4) Weljie, A. M.; Jirik, F. R. Hypoxia-induced metabolic shifts in cancer cells: moving beyond the Warburg effect. *Int. J. Biochem. Cell Biol.* **2011**, *43* (7), 981−989.

(5) Solaini, G.; Baracca, A.; Lenaz, G.; Sgarbi, G. Hypoxia and mitochondrial oxidative metabolism. *Biochim. Biophys. Acta-Bioenergetics* **2010**, *1797* (6−7), 1171−1177.

(6) Guzy, R. D.; Schumacker, P. T. Oxygen sensing by mitochondria at complex III: the paradox of increased reactive oxygen species during hypoxia. *Exp. Physiol.* **2006**, *91* (5), 807−819.

(7) Mylonis, I.; Sembongi, H.; Befani, C.; Liakos, P.; Siniossoglou, S.; Simos, G. Hypoxia causes triglyceride accumulation by HIF-1-mediated stimulation of lipin 1 expression. *J. Cell Sci.* **2012**, *125* (14), 3485−3493.

(8) Mylonis, I.; Simos, G.; Paraskeva, E. Hypoxia-inducible factors and the regulation of lipid metabolism. *Cells* **2019**, *8* (3), 214.

(9) Krishnan, J.; Suter, M.; Windak, R.; Krebs, T.; Felley, A.; Montessuit, C.; Tokarska-Schlattner, M.; Aasum, E.; Bogdanova, A.; Perriard, E.; et al. Activation of a HIF1α-PPARγ axis underlies the integration of glycolytic and lipid anabolic pathways in pathologic cardiac hypertrophy. *Cell Metab.* **2009**, *9* (6), 512−524.

(10) Biron-Shental, T.; Schaiff, W. T.; Ratajczak, C. K.; Bildirici, I.; Nelson, D. M.; Sadovsky, Y. Hypoxia regulates the expression of fatty acid−binding proteins in primary term human trophoblasts. *Am. J. Obstet. Gynecol.* **2007**, *197* (5), 516. e1−516. e6.

(11) Bensaad, K.; Favaro, E.; Lewis, C. A.; Peck, B.; Lord, S.; Collins, J. M.; Pinnick, K. E.; Wigfield, S.; Buffa, F. M.; Li, J.-L.; et al. Fatty acid uptake and lipid storage induced by HIF-1α contribute to cell growth and survival after hypoxia-reoxygenation. *Cell Rep.* **2014**, *9* (1), 349−365.

(12) Hu, B.; Guo, Y.; Garbacz, W. G.; Jiang, M.; Xu, M.; Huang, H.; Tsung, A.; Billiar, T. R.; Ramakrishnan, S. K.; Shah, Y. M.; et al. Fatty acid binding protein-4 (FABP4) is a hypoxia inducible gene that sensitizes mice to liver ischemia/reperfusion injury. *J. Hepatol.* **2015**, *63* (4), 855−862.

(13) Gordon, G. B.; Barcza, M. A.; Bush, M. E. Lipid accumulation in hypoxic tissue culture cells. *Am. J. Pathol.* **1977**, *88* (3), 663.

(14) Thiam, A. R.; Farese, R. V., Jr; Walther, T. C. The biophysics and cell biology of lipid droplets. *Nat. Rev. Mol. Cell Biol.* **2013**, *14* (12), 775−786.

(15) Khor, V. K.; Shen, W.-J.; Kraemer, F. B. Lipid droplet metabolism. *Curr. Opin. Clin. Nutr. Metab. Care* **2013**, *16* (6), 632−637.

(16) Welte, M. A. Expanding roles for lipid droplets. *Curr. Biol.* **2015**, *25* (11), R470−R481.

(17) Baenke, F.; Peck, B.; Miess, H.; Schulze, A. Hooked on fat: the role of lipid synthesis in cancer metabolism and tumour development. *Dis. Model. Mech.* **2013**, *6* (6), 1353−1363.

(18) Cruz, A. L.; Barreto, E. d. A.; Fazolini, N. P.; Viola, J. P.; Bozza, P. T. Lipid droplets: platforms with multiple functions in cancer hallmarks. *Cell Death Dis.* **2020**, *11* (2), 105.

(19) Triantafyllou, E.-A.; Georgatsou, E.; Mylonis, I.; Simos, G.; Paraskeva, E. Expression of AGPAT2, an enzyme involved in the glycerophospholipid/triacylglycerol biosynthesis pathway, is directly regulated by HIF-1 and promotes survival and etoposide resistance of cancer cells under hypoxia. *Biochim. Biophys. Acta, Mol. Cell Biol. Lipids* **2018**, *1863* (9), 1142−1152.

(20) Qiu, B.; Ackerman, D.; Sanchez, D. J.; Li, B.; Ochocki, J. D.; Grazioli, A.; Bobrovnikova-Marjon, E.; Diehl, J. A.; Keith, B.; Simon, M. C. HIF2α-dependent lipid storage promotes endoplasmic reticulum homeostasis in clear-cell renal cell carcinoma. *Cancer Discov.* **2015**, *5* (6), 652−667.
(21) Du, W.; Zhang, L.; Brett-Morris, A.; Aguila, B.; Kerner, J.; Hoppel, C. L.; Puchowicz, M.; Serra, D.; Herrero, L.; Rini, B. I.; et al. HIF drives lipid deposition and cancer in ccRCC via repression of fatty acid metabolism. *Nat. Commun.* **2017**, *8* (1), 1−12.
(22) Huang, D.; Li, T.; Li, X.; Zhang, L.; Sun, L.; He, X.; Zhong, X.; Jia, D.; Song, L.; Semenza, G. L.; et al. HIF-1-mediated suppression of acyl-CoA dehydrogenases and fatty acid oxidation is critical for cancer progression. *Cell Rep.* **2014**, *8* (6), 1930−1942.
(23) Huang, X.; Xue, Z.; Zhang, D.; Lee, H. J. Pinpointing Fat Molecules: Advances in Coherent Raman Scattering Microscopy for Lipid Metabolism. *Anal. Chem.* **2024**, *96*, 7945.
(24) Yue, S.; Li, J.; Lee, S.-Y.; Lee, H. J.; Shao, T.; Song, B.; Cheng, L.; Masterson, T. A.; Liu, X.; Ratliff, T. L.; et al. Cholesteryl ester accumulation induced by PTEN loss and PI3K/AKT activation underlies human prostate cancer aggressiveness. *Cell Metab.* **2014**, *19* (3), 393−406.
(25) Du, J.; Su, Y.; Qian, C.; Yuan, D.; Miao, K.; Lee, D.; Ng, A. H.; Wijker, R. S.; Ribas, A.; Levine, R. D.; et al. Raman-guided subcellular pharmaco-metabolomics for metastatic melanoma cells. *Nat. Commun.* **2020**, *11* (1), 4830.
(26) Li, J.; Condello, S.; Thomes-Pepin, J.; Ma, X.; Xia, Y.; Hurley, T. D.; Matei, D.; Cheng, J.-X. Lipid desaturation is a metabolic marker and therapeutic target of ovarian cancer stem cells. *Cell Stem Cell* **2017**, *20* (3), 303−314. e5.
(27) Li, J.; Cheng, J.-X. Direct visualization of de novo lipogenesis in single living cells. *Sci. Rep.* **2014**, *4* (1), 6807.
(28) Zhang, C.; Li, J.; Lan, L.; Cheng, J.-X. Quantification of lipid metabolism in living cells through the dynamics of lipid droplets measured by stimulated Raman scattering imaging. *Anal. Chem.* **2017**, *89* (8), 4502−4507.
(29) Jüngst, C.; Winterhalder, M. J.; Zumbusch, A. Fast and long term lipid droplet tracking with CARS microscopy. *J. Biophotonics* **2011**, *4* (6), 435−441.
(30) Zhang, C.; Boppart, S. A. Dynamic signatures of lipid droplets as new markers to quantify cellular metabolic changes. *Anal. Chem.* **2020**, *92* (24), 15943−15952.
(31) Clark, M. G.; Gonzalez, G. A.; Zhang, C. Pulse-Picking Multimodal Nonlinear Optical Microscopy. *Anal. Chem.* **2022**, *94* (44), 15405−15414.
(32) Clark, M. G.; Gonzalez, G. A.; Luo, Y.; Aldana-Mendoza, J. A.; Carlsen, M. S.; Eakins, G.; Dai, M.; Zhang, C. Real-time precision opto-control of chemical processes in live cells. *Nat. Commun.* **2022**, *13* (1), 4343.
(33) van Vliet, A. R.; Giordano, F.; Gerlo, S.; Segura, I.; Van Eygen, S.; Molenberghs, G.; Rocha, S.; Houcine, A.; Derua, R.; Verfaillie, T.; et al. The ER stress sensor PERK coordinates ER-plasma membrane contact site formation through interaction with filamin-A and F-actin remodeling. *Mol. Cell* **2017**, *65* (5), 885−899. e6.
(34) Harding, H. P.; Ron, D. Endoplasmic reticulum stress and the development of diabetes: a review. *Diabetes* **2002**, *51*, S455−S461.
(35) Guha, P.; Kaptan, E.; Gade, P.; Kalvakolanu, D. V.; Ahmed, H. Tunicamycin induced endoplasmic reticulum stress promotes apoptosis of prostate cancer cells by activating mTORC1. *Oncotarget* **2017**, *8* (40), 68191.
(36) Wouters, B. G.; Koritzinsky, M. Hypoxia signalling through mTOR and the unfolded protein response in cancer. *Nat. Rev. Cancer* **2008**, *8* (11), 851−864.
(37) Waypa, G. B.; Marks, J. D.; Guzy, R.; Mungai, P. T.; Schriewer, J.; Dokic, D.; Schumacker, P. T. Hypoxia triggers subcellular compartmental redox signaling in vascular smooth muscle cells. *Circ. Res.* **2010**, *106* (3), 526−535.
(38) Sgarbi, G.; Gorini, G.; Liuzzi, F.; Solaini, G.; Baracca, A. Hypoxia and IF1 expression promote ROS decrease in cancer cells. *Cells* **2018**, *7* (7), 64.
(39) Mahapatra, S.; Ma, S.; Dong, B.; Zhang, C. Quantification of cellular phototoxicity of organelle stains by the dynamics of microtubule polymerization. *VIEW* **2024**, No. 20240013.
(40) Szymanski, K. M.; Binns, D.; Bartz, R.; Grishin, N. V.; Li, W.-P.; Agarwal, A. K.; Garg, A.; Anderson, R. G.; Goodman, J. M. The lipodystrophy protein seipin is found at endoplasmic reticulum lipid droplet junctions and is important for droplet morphology. *Proc. Natl. Acad. Sci. U. S. A.* **2007**, *104* (52), 20890−20895.
(41) Wang, H.; Becuwe, M.; Housden, B. E.; Chitraju, C.; Porras, A. J.; Graham, M. M.; Liu, X. N.; Thiam, A. R.; Savage, D. B.; Agarwal, A. K.; et al. Seipin is required for converting nascent to mature lipid droplets. *eLife* **2016**, *5*, No. e16582.
(42) Guo, D.; Hu, L.; Xie, P.; Sun, P.; Yu, W. Seipin is involved in oxygen-glucose deprivation/reoxygenation induced neuroinflammation by regulating the TLR3/TRAF3/NF-κB pathway. *Int. Immunopharmacol.* **2024**, *134*, No. 112182.
(43) Hubbi, M. E.; Semenza, G. L. Regulation of cell proliferation by hypoxia-inducible factors. *Am. J. Physiol. Cell Physiol.* **2015**, *309* (12), C775−C782.
(44) Pistollato, F.; Rampazzo, E.; Persano, L.; Abbadi, S.; Frasson, C.; Denaro, L.; D'Avella, D.; Panchision, D. M.; Puppa, A. D.; Scienza, R.; et al. Interaction of hypoxia-inducible factor-1α and Notch signaling regulates medulloblastoma precursor proliferation and fate. *Stem Cells* **2010**, *28* (11), 1918−1929.
(45) Figueroa, B.; Xu, F. X.; Hu, R.; Men, S.; Fu, D. Quantitative imaging of intracellular density with ratiometric stimulated Raman scattering microscopy. *J. Phys. Chem. B* **2022**, *126* (39), 7595−7603.
(46) Fu, D.; Yu, Y.; Folick, A.; Currie, E.; Farese, R. V., Jr; Tsai, T.-H.; Xie, X. S.; Wang, M. C. *In vivo* metabolic fingerprinting of neutral lipids with hyperspectral stimulated Raman scattering microscopy. *J. Am. Chem. Soc.* **2014**, *136* (24), 8820−8828.
(47) Zhang, W.; Li, Y.; Fung, A. A.; Li, Z.; Jang, H.; Zha, H.; Chen, X.; Gao, F.; Wu, J. Y.; Sheng, H.; et al. Multi-molecular hyperspectral PRM-SRS microscopy. *Nat. Commun.* **2024**, *15* (1), 1599.
(48) Hislop, E. W.; Tipping, W. J.; Faulds, K.; Graham, D. Label-free imaging of lipid droplets in prostate cells using stimulated Raman scattering microscopy and multivariate analysis. *Anal. Chem.* **2022**, *94* (25), 8899−8908.
(49) Wang, P.; Liu, B.; Zhang, D.; Belew, M. Y.; Tissenbaum, H. A.; Cheng, J. X. Imaging lipid metabolism in live *Caenorhabditis elegans* using fingerprint vibrations. *Angew. Chem. Int. Ed* **2014**, *126* (44), 11981−11986.
(50) Huang, K.-C.; Li, J.; Zhang, C.; Tan, Y.; Cheng, J.-X. Multiplex stimulated Raman scattering imaging cytometry reveals lipid-rich protrusions in cancer cells under stress condition. *iScience* **2020**, *23* (3), 100953.
(51) Tantipolphan, R.; Rades, T.; Strachan, C.; Gordon, K.; Medlicott, N. Analysis of lecithin−cholesterol mixtures using Raman spectroscopy. *J. Pharm. Biomed. Anal.* **2006**, *41* (2), 476−484.
(52) Lee, H. J.; Li, J.; Vickman, R. E.; Li, J.; Liu, R.; Durkes, A. C.; Elzey, B. D.; Yue, S.; Liu, X.; Ratliff, T. L.; et al. Cholesterol esterification inhibition suppresses prostate cancer metastasis by impairing the Wnt/β-catenin pathway. *Mol. Cancer Res.* **2018**, *16* (6), 974−985.
(53) Czamara, K.; Majzner, K.; Pacia, M. Z.; Kochan, K.; Kaczor, A.; Baranska, M. Raman spectroscopy of lipids: a review. *J. Raman Spectrosc.* **2015**, *46* (1), 4−20.
(54) Ackerman, D.; Tumanov, S.; Qiu, B.; Michalopoulou, E.; Spata, M.; Azzam, A.; Xie, H.; Simon, M. C.; Kamphorst, J. J. Triglycerides promote lipid homeostasis during hypoxic stress by balancing fatty acid saturation. *Cell Rep.* **2018**, *24* (10), 2596−2605. e5.

https://doi.org/10.1021/cbmi.4c00050
Chem. Biomed. Imaging 2025, 3, 25−34